Application of chaos theory to the particle dynamics of asymmetry-induced transport

D. L. Eggleston
Physics Department, Occidental College, Los Angeles, California 90041, USA

(Received 29 November 2017; accepted 28 February 2018; published online 16 March 2018)

The techniques of chaos theory are employed in an effort to better understand the complex single-particle dynamics of asymmetry-induced transport in non-neutral plasmas. The dynamical equations are re-conceptualized as describing time-independent trajectories in a four-dimensional space consisting of the radius r, rotating frame angle ψ, axial position z, and axial velocity v. Results include the identification of an integral of the motion, fixed-point analysis of the dynamical equations, the construction and interpretation of Poincaré sections to visualize the dynamics, and, for the case of chaotic motion, numerical calculation of the largest Lyapunov exponent. Chaotic cases are shown to be associated with the overlap of resonance islands formed by the applied asymmetry. *Published by AIP Publishing.* https://doi.org/10.1063/1.5017710

I. INTRODUCTION

The cylindrical Malmberg-Penning non-neutral plasma trap provides a suitable platform for fundamental studies of plasma transport since its excellent confinement can be perturbed and the resulting transport studied in a controlled manner. There have been many such experiments[1–11] that use applied non-axisymmetric electric or magnetic fields (i.e., field asymmetries) as the perturbation. These asymmetries produce radial drifts that result in measurable radial transport, but it has been difficult to produce a matching local transport theory. Early attempts to model this transport resulted in resonant particle transport theory,[12] but comparisons between this theory and experiments[7] did not show agreement. To determine the missing physics, we have previously studied the asymmetry-induced dynamics[13] and the resulting transport[14,15] using a single-particle computer code. These studies revealed motions that cannot be described by a simple perturbation theory. In addition to lab-frame trapped particle populations, there were indications of chaotic motion. In this paper, we apply some of the methodologies of chaos theory to single-particle dynamics in our trap in an effort to better characterize these dynamics.

The study of chaos is a mature and multi-faceted field as witnessed by the number of texts on this topic.[16–22] Thus, before beginning, is it helpful to orient ourselves. Chaos studies can be divided into two categories, those involving discrete time steps (often called mappings and based on iterative equations) and those involving time as a continuous variable and based on differential equations. While the study of mappings is interesting and elegant, in our case, where the starting point is the differential equations of motion, it is not of much use since the determination of the map requires the prior solution of the equations of motion. This brings us to the second category, studies based on differential equations. These can be subdivided into studies of dissipative systems and non-dissipative (or *conservative*) systems depending on the evolution in time of a hypervolume in the n-dimensional space formed by the dynamical variables.[23] For a dissipative system, such a hypervolume shrinks in time to some lesser-dimensional object (point, line, plane, fractal) called an attractor. For a conservative system, the hypervolume remains constant, but may change shape, stretching, and contracting in complicated ways. Conservative systems do not have attractors. As we note below, there is a simple test to determine if a system is dissipative or conservative. Finally, we note that systems that can be cast in Hamiltonian form are a subset of conservative systems, and that the existence of quantities that remain constant on trajectories (i.e., constants of the motion) can occur for either dissipative or conservative systems.

We now turn to our problem. We want to model single-particle motions in our modified Malmberg-Penning trap in which the usual non-neutral plasma column has been replaced by a biased wire running along the axis of the trap (see Fig. 1). Low density electrons injected into the trap are subjected to an electric field asymmetry produced by variable-frequency voltages applied to the forty wall sectors. Due to the low electron density, the asymmetry potentials in the trap are essentially the vacuum potentials. The biased center wire produces a symmetric radial electric field which produces an azimuthal $E \times B$ drift similar to that occurring in higher density traps. Additional details have been given in previous papers.[5,7]

The geometry of our trap is cylindrical, so the usual cylindrical coordinates (r, θ, z) are natural, with the z origin at one end of the confinement region of length L and radius R. With the confining magnetic field in the $\hat{z}$-direction, the governing equations of motion are

$$\begin{aligned} \dot{r} &= \frac{1}{B} E_\theta(r, \theta, z, t) \\ \dot{\theta} &= -\frac{1}{rB} E_r(r, \theta, z, t) \\ \ddot{z} &= \frac{q}{m} E_z(r, \theta, z, t). \end{aligned} \tag{1}$$

Here, we have used the drift approximation for $\dot{r}$ and $\dot{\theta}$, whereas $\ddot{z}$ is simply given by Newton's second law. The components of the electric field are derivatives of the potential which we take to be made up of a radially dependent part

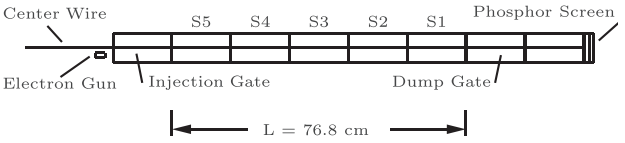

FIG. 1. Schematic of the Occidental College Trap. The usual non-neutral plasma column is replaced by a biased wire that produces an azimuthal $E \times B$ drift similar to that found in other devices. The five cylinders labeled S1–S5 are divided azimuthally into eight sectors each. These forty wall sectors are biased to create an asymmetric field that causes radial transport of the low density electrons injected from an off-axis gun.

$\phi_0(r)$ produced by the center wire bias and an asymmetry potential $\phi_1(r, \theta, z, t)$. These will be specified later.

Chaos theory takes a geometric approach to dynamics by studying trajectories in an abstract n-dimensional space.[16] To this end, the equations of motion are cast as n first-order autonomous differential equations for n dynamical variables x_i

$$\begin{aligned} \dot{x}_1 &= f_1(x_1, \ldots, x_n) \\ &\vdots \\ \dot{x}_n &= f_n(x_1, \ldots, x_n), \end{aligned} \tag{2}$$

or, in n-vector form, $\dot{\mathbf{x}} = \mathbf{f}(\mathbf{x})$. The n dynamical variables define a point in an n-dimensional space referred to as state space or, in the context of Hamiltonian dynamics, phase space. In addition, the n differential equations define a unique direction for the trajectory at that point. The fact that the differential equations are autonomous (i.e., without explicit time dependence) means that the trajectories are time-independent. One can categorize such a system as dissipative or conservative by calculating the appropriate n-dimensional divergence $\nabla \cdot \mathbf{f}$. If this quantity is zero, the system is conservative, and, if less than zero, dissipative.[16,20,24]

To cast our equations in this form, we introduce the axial velocity $v = \dot{z}$ and note that in our experiment the variables θ and t come in the combination $\omega t - l\theta \equiv -l\psi$, where ω is the frequency of the applied asymmetry. Writing the components of the electric field in terms of derivatives of the potential ϕ, we obtain

$$\begin{aligned} \dot{r} &= -\frac{1}{rB}\frac{\partial \phi}{\partial \psi}(r, \psi, z) \\ \dot{\psi} &= -\frac{\omega}{l} + \frac{1}{rB}\frac{\partial \phi}{\partial r}(r, \psi, z) \\ \dot{v} &= -\frac{q}{m}\frac{\partial \phi}{\partial z}(r, \psi, z) \\ \dot{z} &= v. \end{aligned} \tag{3}$$

Thus, our dynamics can be viewed as trajectories in the four-dimensional space formed by r, ψ, z, and v. The $\nabla \cdot \mathbf{f}$ test shows that the system conserves state space volume. In addition, note that the quantity

$$E = \frac{1}{2}mv^2 + q\phi(r, \psi, z) - \frac{q\omega B}{2l}r^2 \tag{4}$$

is a constant of the motion, as can be verified by calculating $\dot{E}$ and using Eq. (3). This means that the trajectories are constrained to remain on constant E 3-D hypersurfaces in the 4-D state space.

We also note that our equations of motion can also be cast in Lagrangian or Hamiltonian form. The appropriate Lagrangian is

$$\mathcal{L}(r, \psi, z, \dot{r}, \dot{\psi}, \dot{z}) = \frac{1}{2}m(\dot{z})^2 - q\phi(r, \psi, z) + \frac{qBr^2}{2}\left(\frac{\omega}{l} + \dot{\psi}\right). \tag{5}$$

One can easily verify that Lagrange's equations for the variables r, ψ, and z reproduce the equations for $\dot{r}$, $\dot{\psi}$, and $\dot{z}$ given in Eq. (3). For the Hamiltonian, note that the conjugate momenta are $p_r = \partial\mathcal{L}/\partial\dot{r} = 0$, $p_\psi = \partial\mathcal{L}/\partial\dot{\psi} = qBr^2/2$, and $p_z = \partial\mathcal{L}/\partial\dot{z} = m\dot{z}$, giving

$$\begin{aligned} H(\psi, z, p_\psi, p_z) &= \sum_i p_i q_i - \mathcal{L} \\ &= \frac{1}{2m}p_z^2 + q\phi(p_\psi, \psi, z) - \frac{\omega}{l}p_\psi. \end{aligned} \tag{6}$$

We can thus also view our dynamics as trajectories in the four dimensional phase space formed by ψ, z, p_ψ, and p_z and our system as consisting of two degrees of freedom. The $\nabla \cdot \mathbf{f}$ test gives zero for any Hamiltonian system, thus confirming our previous characterization of the system as conservative. Finally, note that the Hamiltonian is a constant of the motion since it does not depend explicitly on time. By substituting in the expressions for p_z and p_ψ, we again obtain Eq. (4).

II. ANALYTICAL RESULTS

To proceed, we must now specify the form of the potential $\phi(r, \psi, z)$. We use a form that is relevant to our experimental work

$$\phi(r, \psi, z) = \phi_0(r) + \phi_1(r)\cos kz \cos(-l\psi). \tag{7}$$

Here, the cylindrically symmetric potential $\phi_0(r)$ is produced by the biased wire along the axis of the trap, while the second term is a perturbing asymmetric potential produced by appropriately biased wall patches, with k and l being the axial and azimuthal wavenumbers, respectively. This asymmetry is used in the experiments since its simplicity makes comparisons with theory unambiguous; details are given in Ref. 7. Using this potential in Eq. (3) and specifying $q = -e$ gives

$$\begin{aligned} \dot{r} &= -\frac{l}{rB}\phi_1(r)\cos kz \sin(-l\psi) \\ \dot{\psi} &= -\frac{\omega}{l} + \omega_R(r) + \frac{1}{rB}\frac{d\phi_1}{dr}\cos kz \cos(-l\psi) \\ \dot{v} &= -\frac{ek}{m}\phi_1(r)\sin kz \cos(-l\psi) \\ \dot{z} &= v, \end{aligned} \tag{8}$$

where we have defined $\omega_R(r) \equiv \frac{1}{rB}\frac{d\phi_0}{dr}$, the azimuthal rotation frequency produced by the biased center wire.

A. Conditions for chaos

We first note that Eq. (8) satisfies the *necessary conditions* for chaos in a bounded system.[16,20] These are (1) the presence of nonlinearity that couples at least some of the

equations (provided by the terms with sine and cosine functions) and (2) the number of equations minus the number of constants of motion must be greater than or equal to three [we have four equations and one constant given by Eq. (4)]. Interestingly, chaos theory does not yet have a way to determine *sufficient conditions* for chaos.[18] As we shall see, trajectories for our system can be either regular or chaotic depending on initial conditions.

B. Fixed point analysis

We next consider the fixed (or equilibrium) points of Eq. (8), i.e., those points where $\dot{r}$, $\dot{\psi}$, $\dot{z}$, $\dot{v}$ are all zero. While these points constitute a very small portion of state space, their properties often give insights into the larger picture.[17]

From the $\dot{z}$ equation, we see immediately that fixed points require $v=0$. Similarly, from the $\dot{r}$ and $\dot{v}$ equations, $\cos kz \sin(-l\psi)=0$ and $\sin kz \cos(-l\psi)=0$ are required. These can be simultaneously satisfied in two ways: (1) $kz=0$, $\pm\pi$ and $-l\psi=0$, $\pm\pi$ [making $\sin kz$ and $\sin(-l\psi)$ zero] or (2) $kz=\pm\frac{\pi}{2}$ and $-l\psi=\pm\frac{\pi}{2}$ [making $\cos kz$ and $\cos(-l\psi)$ zero]. Here, we have restricted the domain of the sine and cosine functions to $-\pi$ to $+\pi$. Finally, we require $\dot{\psi}=0$ which means that $\omega_R(r)-\frac{\omega}{l}+\frac{1}{rB}\frac{d\phi_1}{dr}\cos kz\cos(-l\psi)=0$. For the case 1 fixed points, this reduces to $\omega_R(r)-\frac{\omega}{l}\pm\frac{1}{rB}\frac{d\phi_1}{dr}=0$ while the case 2 simply requires $\omega_R(r)-\frac{\omega}{l}=0$. Since ϕ_1 is typically small compared to ϕ_0, both of these cases set the requirement that $\omega\approx l\omega_R(r)$, which sets the value of r for the fixed points.

We next examine the stability of the fixed points by considering small displacements δr, $\delta\psi$, δv, and δz from these equilibria. Each of the equalities in Eq. (8) can be Taylor expanded in powers of these displacements. To first order in the displacements, the result can be cast in the matrix form

$$\frac{d}{dt}\begin{pmatrix}\delta r\\ \delta\psi\\ \delta v\\ \delta z\end{pmatrix}=\begin{pmatrix}-C_r\cos kz\sin(-l\psi) & lC\cos kz\cos(-l\psi) & 0 & kC\sin kz\sin(-l\psi)\\ \omega_r+D_r\cos kz\cos(-l\psi) & lD\cos kz\sin(-l\psi) & 0 & -kD\sin kz\cos(-l\psi)\\ -F_r\sin kz\cos(-l\psi) & -lF\sin kz\sin(-l\psi) & 0 & -kF\cos kz\cos(-l\psi)\\ 0 & 0 & 1 & 0\end{pmatrix}\begin{pmatrix}\delta r\\ \delta\psi\\ \delta v\\ \delta z\end{pmatrix}, \tag{9}$$

where $C=\frac{l}{rB}\phi_1(r)$, $D=\frac{l}{rB}\frac{d\phi_1}{dr}$, $F=\frac{ek}{m}\phi_1(r)$, $C_r=\frac{dC}{dr}$, $D_r=\frac{dD}{dr}$, $F_r=\frac{dF}{dr}$, and $\omega_r=\frac{d\omega_R}{dr}$, and where the elements of the 4×4 matrix are evaluated at the fixed point under consideration. If we denote the column vector $(\delta r, \delta\psi, \delta v, \delta z)$ as $\delta\mathbf{r}$ and the matrix as $\mathbf{J}$, we can write Eq. (9) in the compact form

$$\delta\dot{\mathbf{r}}=\mathbf{J}\delta\mathbf{r}. \tag{10}$$

$\mathbf{J}$ is called the Jacobian or stability matrix. Equation (10) can be solved by solving an associated eigenvalue problem.[17] To see this, assume that $\delta\mathbf{r}$ has the form

$$\delta\mathbf{r}=\sum_{i=1}^{4}c_i\mathbf{A_i}e^{\lambda_i t}, \tag{11}$$

where c_i and λ_i are constants and $\mathbf{A_i}$ are constant four-vectors. Then

$$\mathbf{J}\delta\mathbf{r}=\mathbf{J}\sum_{i=1}^{4}c_i\mathbf{A_i}e^{\lambda_i t}=\sum_{i=1}^{4}c_i\mathbf{J}\mathbf{A_i}e^{\lambda_i t}. \tag{12}$$

The last expression is equal to $\delta\dot{\mathbf{r}}$ if $\mathbf{J}\mathbf{A_i}=\lambda_i\mathbf{A_i}$, that is, if $\mathbf{A_i}$ and λ_i are the eigenvector and eigenvalue for the transformation $\mathbf{J}$. The solution of Eq. (10) can thus be found by finding these eigenvectors and eigenvalues and plugging into Eq. (11). The eigenvalues are found by solving the characteristic equation of the matrix $\mathbf{J}$, i.e., the determinant $|\mathbf{J}-\lambda\mathbf{I}|=0$, which, in our case, gives four values λ_i. When each of these values is substituted into the eigenvalue equation, we obtain the corresponding eigenvector $\mathbf{A_i}$.

When the stability matrix is evaluated at the fixed points, the sine and cosine terms will give zero or ±1. For the case 1 fixed points, $\mathbf{J}$ reduces to

$$\begin{pmatrix}0 & lCS & 0 & 0\\ -G & 0 & 0 & 0\\ 0 & 0 & 0 & -kFS\\ 0 & 0 & 1 & 0\end{pmatrix}, \tag{13}$$

where $-G=\omega_r+D_rS$ and the sign parameter $S=1$ when $(kz, -l\psi)$ are either $(0,0)$ or $(\pm\pi, \pm\pi)$, while $S=-1$ when $(kz, -l\psi)$ are either $(0, \pm\pi)$ or $(\pm\pi, 0)$. The resulting eigenvalues are $[-i\sqrt{kFS}, i\sqrt{kFS}, -i\sqrt{lCGS}, i\sqrt{lCGS}]$ with the corresponding eigenvectors $[(0,0,-i\sqrt{kFS},1),(0,0,i\sqrt{kFS},1),(i\sqrt{lCS/G},1,0,0),(-i\sqrt{lCS/G},1,0,0)]$. We first note that, because of the zeros in the eigenvectors, the motion in the r–ψ plane is independent of the motion in the v–z plane. Second, since we have defined C, F, and G to be positive for typical experimental conditions, the character of the case 1 solutions thus depends only on the sign parameter S. For $S=1$ (case 1a), the eigenvalues are all imaginary. Such a fixed point is termed *elliptical* (or *a center*) since the resulting solutions can be cast in the form of ellipses in the r–ψ and v–z planes, with the rate of rotation about the center determined by the appropriate eigenvalue. For $S=-1$ (case 1b), the eigenvalues are all real, giving the so-called *hyperbolic* (or *saddle*) points. Here, the solutions can be cast in the form of hyperbolas in the r–ψ and v–z planes. Analysis of the r–ψ motion shows that the flow is toward the origin in the first and third quadrants of the r–ψ

plane and away from the origin in the second and fourth quadrants. For the v–z motion, the flow directions are reversed.

For the case 2 fixed points, **J** reduces to

$$\begin{pmatrix} 0 & 0 & 0 & kCS \\ -H & 0 & 0 & 0 \\ 0 & -lFS & 0 & 0 \\ 0 & 0 & 1 & 0 \end{pmatrix}, \tag{14}$$

where $-H = \omega_r$ and $S = 1$ when $(kz, -l\psi)$ are either $(\pi/2, \pi/2)$ or $(-\pi/2, -\pi/2)$, while $S = -1$ when $(kz, -l\psi)$ are either $(\pi/2, -\pi/2)$ or $(-\pi/2, \pi/2)$. The resulting eigenvalues are $[-R, -iR, iR, R]$ with the corresponding eigenvectors $[(-Q,-T,-R,1), (iQ,T,-iR,1), (-iQ,T,iR,1), (Q,-T,R,1)]$. Here, we have defined $R = (HkClF)^{1/4}, Q = (k^3C^3/HlF)^{1/4}$, and $T = (HkC/lF)^{1/2}$ for compactness, all of which are real for typical experimental conditions. Note that here the sign parameter S has cancelled out, so all case 2 solutions have the same character. Here, the motion is more difficult to characterize, but the form of the eigenvalues and eigenvectors shows that the motion is fully four-dimensional with a mixture of elliptical and hyperbolic elements. The location and classification of all of the fixed points relative to the asymmetric potential are noted in Fig. 2.

III. NUMERICAL RESULTS

We now turn to results obtained by numerically solving Eq. (8). To do so, we must specify further details of our model. The potential $\phi_0(r)$ is given by $\phi_{cw}\ln(R/r)/\ln(R/a)$, where ϕ_{cw} and a are the bias and radius of the center wire, respectively. The asymmetry potential amplitude function $\phi_1(r)$ is given by $\phi_{10}(r/R)^l$, with ϕ_{10} a constant. This form closely approximates the exact vacuum solution. The axial wavenumber $k = n\pi/L$, with n being an integer. For the results shown in this paper, we use typical experimental values: $B = 364$ G, $\phi_{cw} = -80$ V, $l = k = 1$, $\phi_{10} = 0.2$ V, and $\ln(R/a) = 5.3838$.

Numerical solutions are obtained using Mathematica's NDSOLVE routine.[25] We treat our system as having an infinite extent in z with periodicity $2L$, which is equivalent to assuming specular reflection at the ends of our confinement region of length L. We use the following scalings for our solutions: r is scaled to the wall radius R, z to L, v to $v_0 = 10^6$ cm/s, time t to 10^{-6} s, and frequencies to either 10^6 Hz (for λ) or 10^6 rad/s (for ω).

To check the accuracy of our solutions, we plug the resulting numerical functions for r, ψ, z, and v back into Eq. (8) and take the difference between the two sides. A perfect solution would give zero for each equation. Judicious choices among NDSOLVE's options keep these quantities below 10^{-10} for our solutions, while variations in the constant E are in the range $\delta E/E \approx 10^{-6}$. Our setting are: MaxSteps → ∞, InterpolationOrder → All, AccuracyGoal → 15, PrecisionGoal → 15, Method → StiffnessSwitching.

A. Lyapunov exponent

While the fixed point analysis in Sec. II B gives some indication of the types of motion to expect, we want to be able

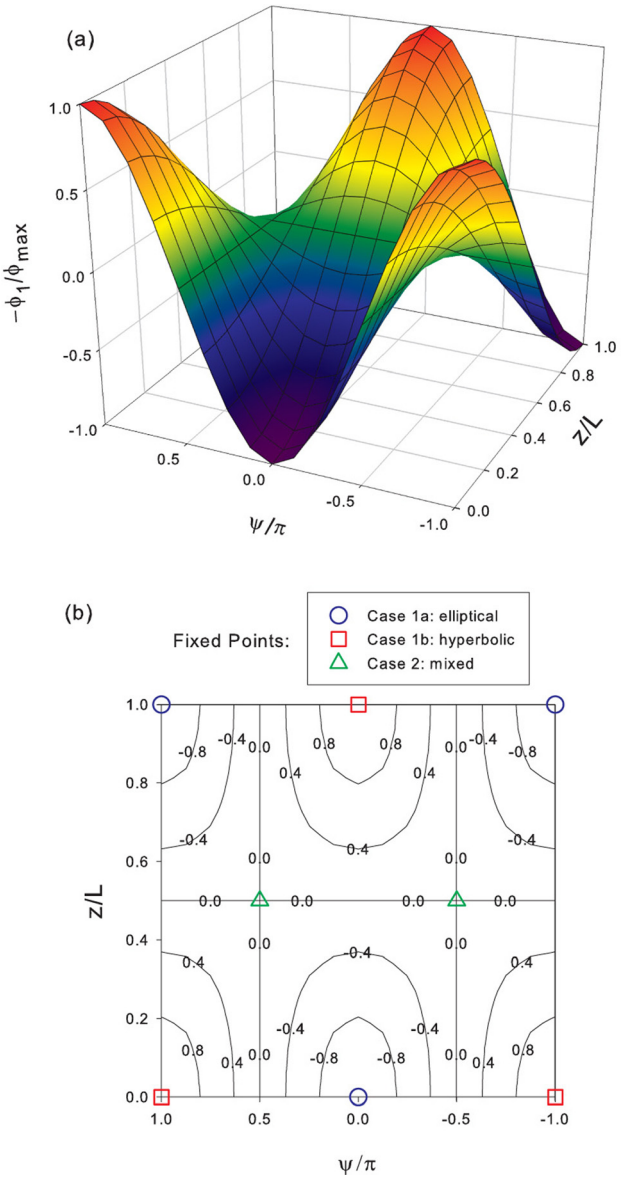

FIG. 2. Location of fixed points relative to the asymmetric potential. (a) 3-D plot of the normalized asymmetry potential. At the fixed point radius, this potential is stationary. (b) Contour plot of the normalized asymmetry potential with the location and classification of the fixed points indicated.

to characterize the motion for an arbitrary initial point in state space. Chaotic dynamics are characterized by the exponential divergence of neighboring initial points. The rate of divergence is given by the Lyapunov exponents, one for each dimension of the state space. The standard conceptual picture is to imagine a point in state space surrounded by a small sphere whose surface represents neighboring initial conditions. As the system evolves, the central point will follow its trajectory, while the surface of the sphere will deform into an ellipsoid as the sphere stretches or contracts along its axes. The average rates of change along the axes are the Lyapunov exponents λ_i, defined by

$$\lambda_i = \lim_{t\to\infty, d_i(0)\to 0}\left[\frac{1}{t}\ln\left(\frac{d_i(t)}{d_i(0)}\right)\right], \tag{15}$$

where $d_i(t)$ is the length of the ellipsoid along the ith axis at time t. The presence of chaos is then indicated by a positive λ_i. While this formal definition is widely quoted, it is not of much use in numerical calculations. Since the motion is bounded, $d_i(t)$ will quickly reach its maximum value, after which the $1/t$ factor will decrease λ_i to zero. An alternate method for calculating the largest Lyapunov exponent was developed by Benettin *et al.*[19,26] The idea is to follow two neighboring trajectories separated by an initial small distance d_0 for a time τ, after which the distance between them is renormalized to its initial small value. The computation is then continued until a time 2τ, at which point the renormalization is repeated, and so on at time intervals of τ. At each multiple k of τ, the partial sum

$$\lambda_k = \frac{1}{k\tau}\sum_{j=1}^{k} \ln\left(\frac{d_j}{d_0}\right) \tag{16}$$

is computed, where d_j is the distance between the two trajectories before normalization. Then, the maximum Lyapunov exponent is given by

$$\lambda = \lim_{k\to\infty} \lambda_k, \tag{17}$$

which can be estimated by plotting λ_k versus k. Example plots are shown in Fig. 3. For both the cases shown, we have taken the initial conditions to be $v = 10$, $\psi = 0$, and $z = -0.05$ and have set the parameter ω to 0.5. The solid circles have initial $r/R = 0.674$, while the open circles have 0.750. The numerical solutions extend only to $k = 4000$, but this is long enough for the first case to show its asymptotic value. The second case continues to fall with increasing k thus implying $\lambda = 0$ [cf. Eq. (17)]. As previously discussed, positive λ indicates chaotic motion, while $\lambda = 0$ occurs for regular motion.

B. Poincaré sections

As an aid in visualizing trajectories in our four-dimensional state space, we employ Poincaré surface of sections. In our case, these are constructed by noting the values of r, ψ, and v whenever the trajectory passes $z = 0$ (or integer multiple of $2L$) with a positive velocity. The code is run to $t = 6000$ to get a reasonable number of points. Longer runs make it difficult to distinguish between the different symbols and do not add significantly to the patterns shown. We then plot the normalized values of ψ versus r (with ψ constrained to be between $-\pi$ and π) and v versus r. The resulting plots depend on the selected initial conditions and the parameter ω. Representative examples are shown in Figs. 4, 5, and 6 for ω values of 0.5, 0.35, and 2.0 and initial v values of 10, 5, and 5, respectively. Common initial conditions are $\psi = 0$ and $z = -0.05$, and we plot several initial values of r/R on the same graph. The legend gives these initial r/R values and the value of λ_k at the end of the solution. For simplicity, we consider any $\lambda_k \le 0.007$ to be zero, indicating regular (i.e., non-chaotic) motion. This somewhat arbitrary cutoff value is in accordance with the behavior seen in Fig. 3 and the amount of scatter in the Poincaré sections.

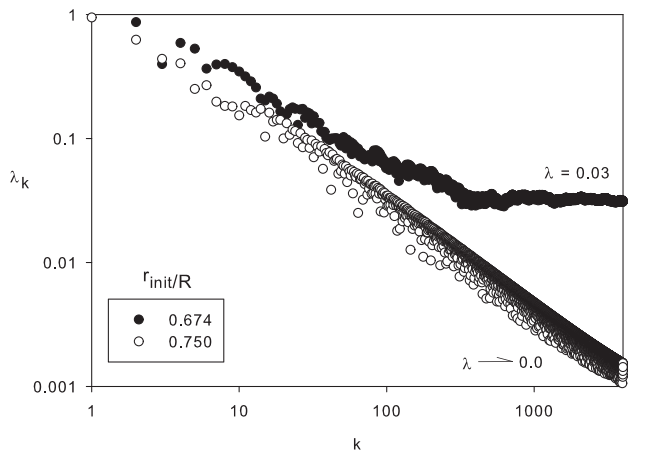

FIG. 3. Obtaining the Lyapunov exponent for two different initial values of r/R using the method of Ref. 26.

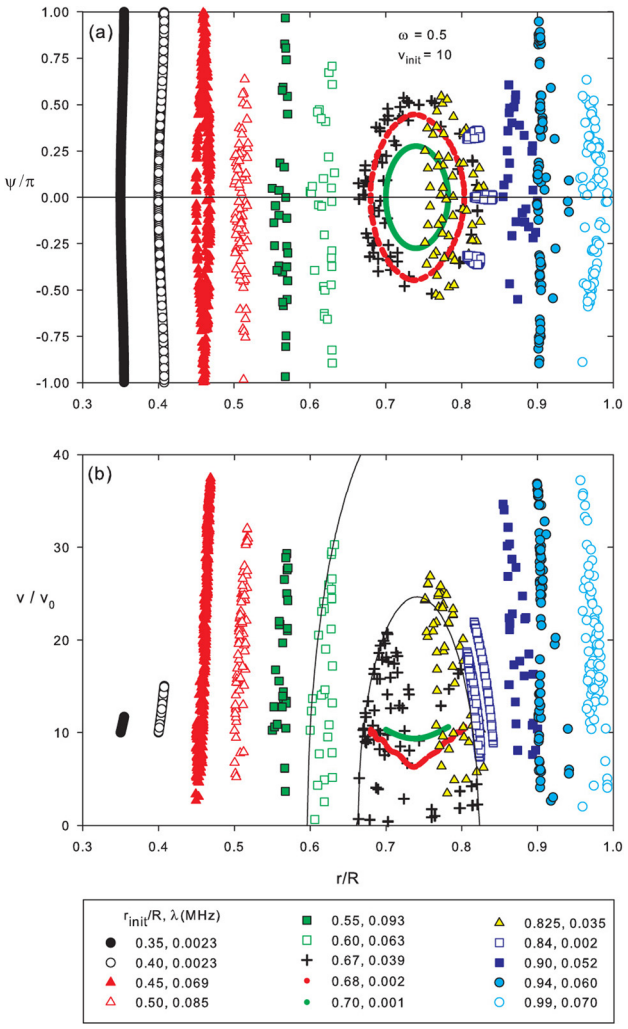

FIG. 4. Poincaré sections taken at the $z = 0$ crossing for fourteen different initial r/R values through time $t = 6000$ for $\omega = 0.5$ and $v_{init} = 10$. The legend shows the initial r/R values and the corresponding Lyapunov exponent λ. Values of λ below 0.007 should be considered to be zero and to indicate regular motion. (a) Plot of normalized ψ versus r. The elliptically shaped curves centered on $r/R \approx 0.74$ are due to axially trapped particles. (b) Plot of normalized v versus r for the same set of initial r values. The solid lines show the maximum possible velocity for two representative initial radii: $r/R = 0.60$ and $r/R = 0.67$.

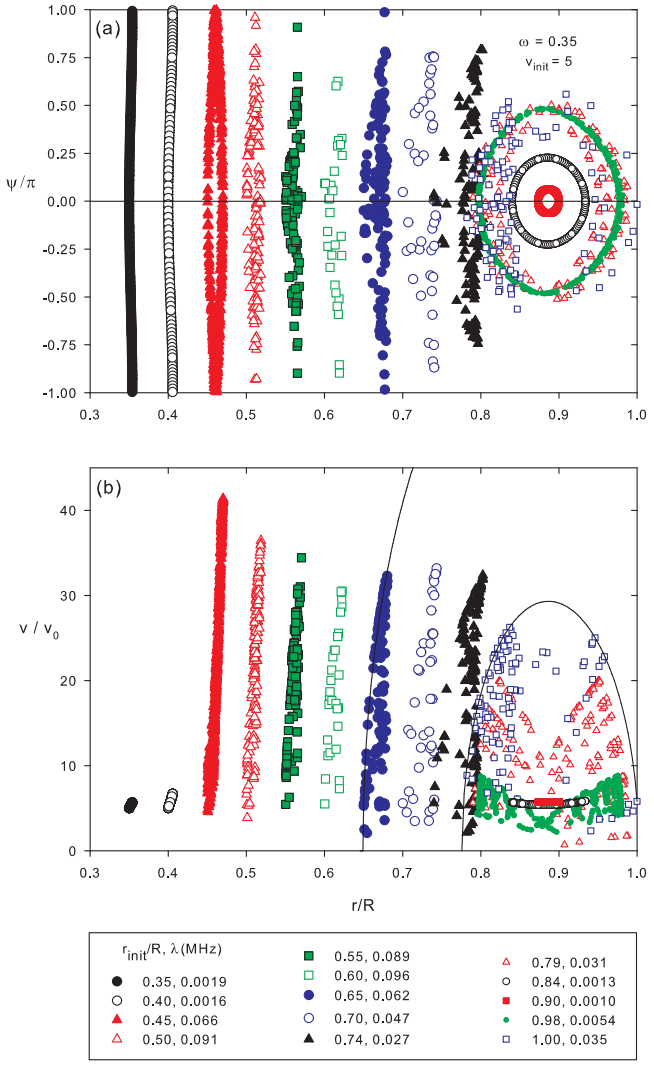

FIG. 5. Poincaré sections taken at the $z=0$ crossing for fourteen different initial r/R values through time $t=6000$ for $\omega=0.35$ and $v_{init}=5$. The legend shows the initial r/R values and the corresponding Lyapunov exponent λ. Values of λ below 0.007 should be considered to be zero and to indicate regular motion. (a) Plot of normalized ψ versus r. The elliptically shaped curves centered on $r/R\approx 0.88$ are due to axially trapped particles. (b) Plot of normalized v versus r for the same set of initial r values. The solid lines show the maximum possible velocity for two representative initial radii: $r/R=0.65$ and $r/R=1.00$.

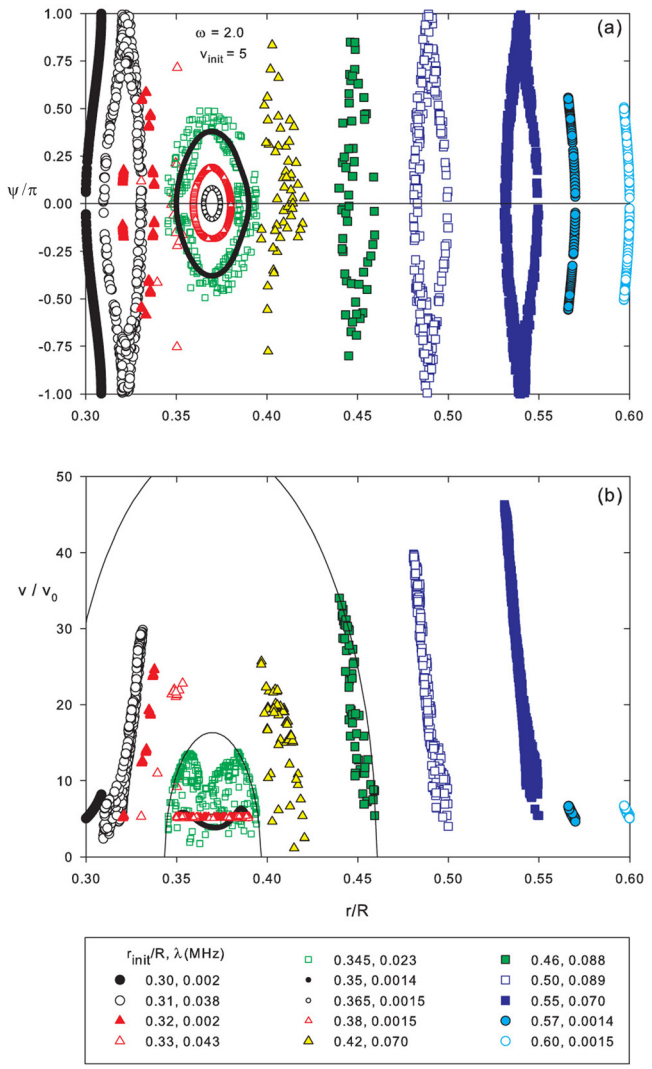

FIG. 6. Poincaré sections taken at the $z=0$ crossing for fourteen different initial r/R values through time $t=6000$ for $\omega=2.0$ and $v_{init}=5$. The legend shows the initial r/R values and the corresponding Lyapunov exponent λ. Values of λ below 0.007 should be considered to be zero and to indicate regular motion. (a) Plot of normalized ψ versus r. The elliptically shaped curves centered on $r/R\approx 0.37$ are due to axially trapped particles. (b) Plot of normalized v versus r for the same set of initial r values. The solid lines show the maximum possible velocity for two representative initial radii: $r/R=0.345$ and $r/R=0.46$.

The Poincaré sections have a number of interesting features. Looking first at the ψ versus r plots, we note the presence of the closed elliptically shaped curves centered at $r/R\approx 0.74$, 0.88, and 0.37 in Figs. 4, 5, and 6, respectively. These centers are the elliptical fixed points found in Sec. II B with the radius of the center given by $\omega\approx l\omega_R(r)$. We have verified this conclusion by producing Poincaré sections for a wide range of ω values. Examination of the full time record (r, ψ, z, and v versus t) shows that these ellipses are formed by the regular motion of particles that are axially trapped in the asymmetry potential. The large radial excursions of these particles make them especially interesting for transport studies. By varying the initial radius and the amplitude of the asymmetry ϕ_{10}, we find that the largest ellipse has a full radial excursion (largest r minus smallest r) given by $\Delta r/R \approx 0.21(r_0/R)^{1.5}(\phi_{10}(\mathrm{V})/0.2)^{0.5}$, where r_0 is the location of the center. This is the same scaling as that for a particle with oscillating $\vec{E}\times\vec{B}$ radial velocity $v_r=v_{r0}\sin\omega_0 t$, i.e., $\Delta r=2v_{r0}/\omega_0$ where $\omega_0\approx\sqrt{lCG}$ is the frequency for r–ψ motion around the elliptical fixed point found in Sec. II B.

At initial r values just outside of the largest ellipse boundary, we see chaotic particles that also have large radial excursions. The full time record here shows that these particles switch from being axially trapped to passing in an irregular way. The behavior is highly sensitive to the initial v value. At the remaining r_{init} values, we see both regular and chaotic cases with varying amounts of radial motion. Notable are the points lying on the flattened, elongated curves [e.g., $r_{init}/R=0.45$ in Fig. 4(a)]. These seem to occur when particles are interacting resonantly with one of the two counter-propagating helical waves that make up our asymmetry (see the discussion below in Sec. III C). Note that in Fig. 6(a) that the radial excursions

for these cases are comparable to that for the axially trapped particles.

Turning now to the v versus r plots, we first note that the different initial r values give differing amounts of v variation, and, in some cases, the amount of v variation can be very large compared to the initial value. For example, in Fig. 5(b) the velocity varies from its initial value of 5 to over 40 for the $r_{init}/R = 0.45$ case. Generally, the amount of v variation shown is related to the amplitude of the radial excursions since the E value given in Eq. (4) is constant and set by the initial conditions. Equation (4) has a minimum at the fixed point radius, so particles to the left of the fixed point increase their velocity as they move to larger radii, while particles to the right of the fixed point increase their velocity as they move to smaller radii. To illustrate this, we have plotted solid lines showing v versus r derived from Eq. (4) for two representative cases on each plot. This line shows the maximum v value possible as the particle moves radially. The points plotted are on or below this line since the value of ψ varies for the Poincaré sections.

An apparent exception to this general picture seems to be the axially trapped particles which show little variation in v despite their large radial excursions. This is due to two effects. First, the axially trapped particles are near the minimum of E so radial excursions do not produce as much v variation as they do at other radii. Second, the regular, oscillatory motion of the axially trapped particles correlates the v and z motions of the particles; since the Poincaré sections are taken at a fixed value of z, the variations in v are reduced.

Finally, we note that the chaotic cases shown in Figs. 4, 5, and 6 have λ in the range 23–96 kHz which introduces a time scale for collisionless mixing of the orbits that is comparable to other characteristic time scales for this system (azimuthal rotation and axial bounce times). We have not yet explored the importance of this, but similar situations have been noted in the astrophysics literature to have significant effects.[22,27] The effect of chaos on transport in plasmas has been studied for some time[28] but it has not, to our knowledge, been considered in the context of non-neutral plasmas.

C. Resonance overlap

The observed occurrence of a mixture of both regular and chaotic motion is common in conservative systems but raises the question of why certain initial conditions give chaotic or regular motion. The answer appears to be related to the Chirikov resonance overlap condition.[21,29,30] To see this, first note that our asymmetry can be decomposed into two equal amplitude counter-propagating helical waves

$$\phi_1(r)\cos kz\cos(-l\psi) = \frac{\phi_1(r)}{2}[\cos(kz - l\psi) + \cos(-kz - l\psi)]. \tag{18}$$

The two helical waves have resonant velocities $\pm v_{res}$ where

$$v_{res} = \frac{l\omega_R(r) - \omega}{k}. \tag{19}$$

These resonant velocities vary with radius and are shown by the solid lines in Fig. 7. Particles moving with either helical wave are trapped in its potential and oscillate around v_{res} at the trapping frequency[13]

$$\omega_T = \sqrt{\left(\frac{e}{m}k^2 - \frac{l^2}{rB}\frac{d\omega_R}{dr}\right)\phi_1(r)}. \tag{20}$$

These oscillations form resonance islands with half-width $\Delta v = 2\omega_T/k$. The boundaries of these islands are shown by the dashed lines in Fig. 7.

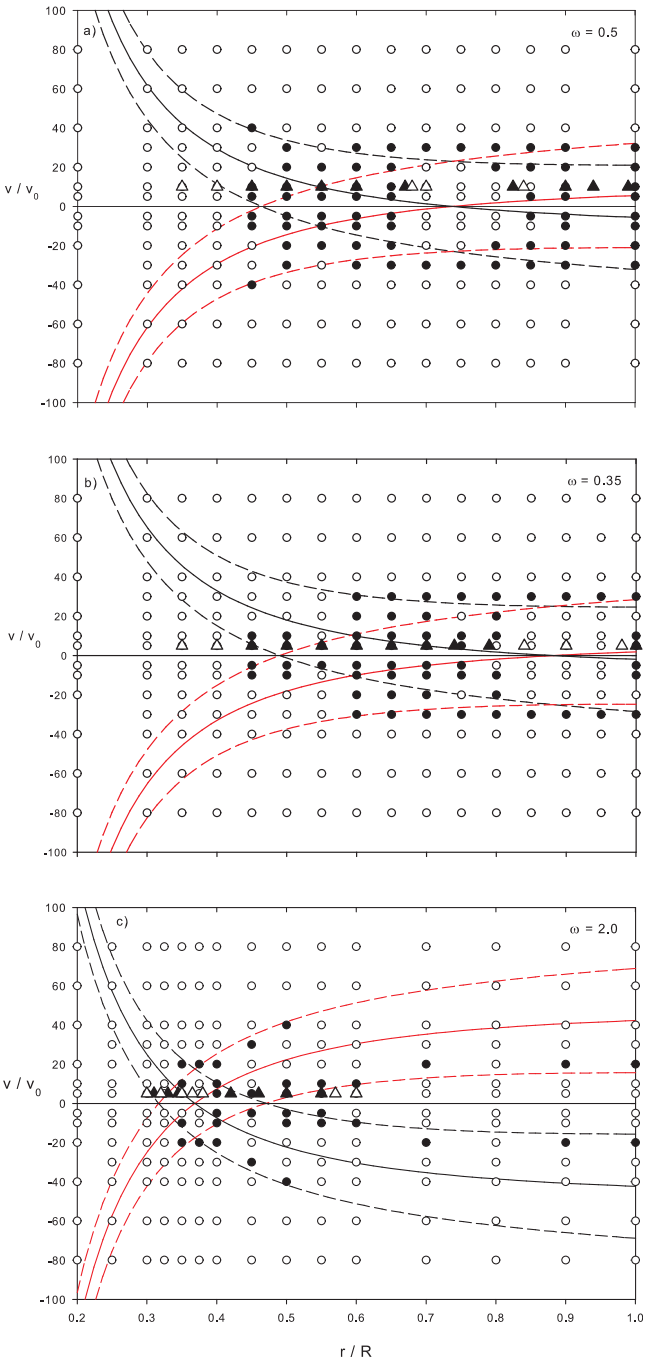

FIG. 7. Plot of the resonant velocity (solid lines) and the resonant island boundaries (dashed lines) for the two helical waves constituting the asymmetric potential. In addition, filled (unfilled) symbols are plotted for initial (r, v) values giving chaotic (regular) motion. Triangular symbols are used for initial conditions matching those in Figs. 4, 5, and 6. This is done for (a) $\omega = 0.5$, (b) $\omega = 0.35$, and (c) $\omega = 2.0$ to show the association of chaotic cases with resonance overlap.

We now add to the plot the results of Lyapunov exponent calculations for a variety of initial r and v values; initial z and ψ are held constant with value zero. Cases giving $\lambda_k \geq 0.007$ are considered chaotic and plotted with a filled symbol, while regular motion is indicated by an unfilled symbol. The initial conditions producing Figs. 4, 5, and 6 are plotted with triangular symbols.

The pattern seen is that the chaotic cases are associated with the helical resonances. They are found where the two resonance islands are close together or overlapping, or where an initial condition is close to a resonance island boundary. This pattern is similar to that found in other systems where chaos is associated with resonance overlap.[21,29,30]

A notable exception to this picture occurs in our system near the point where the two resonant velocities cross (i.e., where $v_{res} = 0$). Even though the two resonance islands are fully overlapping, the motion is regular. This is due to the fact that these initial conditions are near the elliptical fixed point ($\omega = \omega_R$) and the associated axially trapped, oscillatory motion which limits the divergence of neighboring initial conditions.

IV. CONCLUSIONS

We have characterized the motion of particles in our cylindrical Malmberg-Penning trap using some of the tools of chaos theory. The problem was re-conceptualized as describing motion on a three-dimensional hypersurface in a four-dimensional space with one constant of the motion. Fixed point analysis reveals elliptical, hyperbolic, and mixed behaviors. We used the technique of Benettin *et al*. to calculate Lyapunov exponents which show that both regular and chaotic motion occur in our system, and this was illustrated with example Poincaré sections. The chaotic cases were shown to be associated with the overlap of resonance islands formed by the applied asymmetry. It is hoped that these studies of particle dynamics will aid the development of the correct local theory for asymmetry-induced transport.

ACKNOWLEDGMENTS

The author acknowledges the assistance of Kayla Currier and Quinn Taylor and support from Occidental College.

[1]D. L. Eggleston, T. M. O'Neil, and J. H. Malmberg, Phys. Rev. Lett. **53**, 982 (1984).
[2]J. Notte and J. Fajans, Phys. Plasmas **1**, 1123 (1994).
[3]X.-P. Huang, F. Anderegg, E. M. Hollman, C. F. Driscoll, and T. M. O'Neil, Phys. Rev. Lett. **78**, 875 (1997).
[4]J. M. Kriesel and C. F. Driscoll, Phys. Rev. Lett. **85**, 2510 (2000).
[5]D. L. Eggleston and B. Carrillo, Phys. Plasmas **9**, 786 (2002).
[6]E. Gilson and J. Fajans, Phys. Rev. Lett. **90**, 015001 (2003).
[7]D. L. Eggleston and B. Carrillo, Phys. Plasmas **10**, 1308 (2003).
[8]A. A. Kabantsev, J. H. Yu, R. B. Lynch, and C. F. Driscoll, Phys. Plasmas **10**, 1628 (2003).
[9]J. R. Danielson and C. M. Surko, Phys. Plasmas **13**, 055706 (2006).
[10]Y. Soga, Y. Kiwamoto, and N. Hashizume, Phys. Plasmas **13**, 052105 (2006).
[11]A. A. Kabantsev, D. H. E. Dubin, C. F. Driscoll, and Y. A. Tsidulko, Phys. Rev. Lett. **105**, 205001 (2010).
[12]D. L. Eggleston and T. M. O'Neil, Phys. Plasmas **6**, 2699 (1999).
[13]D. L. Eggleston, Phys. Plasmas **14**, 012302 (2007).
[14]D. L. Eggleston, Phys. Plasmas **19**, 042307 (2012).
[15]D. L. Eggleston, Phys. Plasmas **21**, 072318 (2014).
[16]G. L. Baker and J. P. Gollub, *Chaotic Dynamics an Introduction* (Cambridge University Press, New York, 1990), p. 3.
[17]M. Tabor, *Chaos and Integrability in Nonlinear Dynamics: An Introduction* (Wiley, New York, 1989), pp. 20–25.
[18]M. Lakshmanan and S. Rajasekar, *Nonlinear Dynamics: Integrability, Chaos, and Patterns* (Springer, New York, 2003), p. 148.
[19]A. J. Lichtenberg and M. A. Lieberman, *Regular and Chaotic Dynamics*, 2nd ed. (Springer-Verlag, New York, 1992), pp. 296–302.
[20]S. H. Strogatz, *Nonlinear Dynamics and Chaos* (Westview Press, Boulder, Colorado, 2015), p. 212.
[21]Y. Elskens and D. Escande, *Microscopic Dynamics of Plasma and Chaos* (Institute of Physics Publishing, Bristol, 2003), pp. 103–111, 133–139.
[22]G. Contopoulos, *Order and Chaos in Dynamical Astronomy* (Springer, New York, 2004), pp. 508–513.
[23]References 16, 19, and 22 use the term *conservative* in this way since the phase space volume is conserved in a non-dissipative system. It should be noted, however, that some authors[17,20] use the term *conservative* to describe systems that have one or more quantities that are constant on trajectories. While there are some systems (e.g. Hamiltonian systems with $\partial H/\partial t = 0$) that satisfy both definitions, this is not always the case.
[24]L. N. Hand and J. D. Finch, *Analytical Mechanics* (Cambridge University Press, New York, 1998), pp. 18418–18419.
[25]Wolfram Research, Inc., Mathematica, Version 11.0, Champaign, IL (2016).
[26]G. Benettin, L. Galgani, and J.-M. Strelcyn, Phys. Rev. A **14**, 2338 (1976); G. Benettin and J.-M. Strelcyn, *ibid.* **17**, 773 (1978); G. Benettin, L. Galgani, A. Giorgilli, and J.-M. Strelcyn, Meccanica **15**, 9 (1980).
[27]D. Pfenniger, Astron. Astrophys. **165**, 74 (1986).
[28]See, for example, G. M. Zaslavsky, Phys. Rep. **371**, 461 (2002), and references contained therein.
[29]B. V. Chirikov, Phys. Rep. **52**, 263 (1979).
[30]D. F. Escande, Phys. Scr. T **2/1**, 126–141 (1982).